Inelastic scattering of electron vortices on crystals

Jan Rusz[1,2] and Somnath Bhowmick[1,3]

[1]*Department of Physics and Astronomy, Uppsala University, P.O. Box 516, 75120 Uppsala, Sweden*
[2]*Institute of Physics, Czech Academy of Sciences,*
Na Slovance 2, CZ-182 21 Prague, Czech Republic
[3]*Indian Institute of Technology, Kanpur, India*

Electron vortex beams (EVB), that is electron beams carrying an orbital angular momentum, are a novel development in the field of transmission electron microscopy. Among their possible applications, a recent experiment indicated that they may enable measurements of the electron magnetic circular dichroism (EMCD) with much better signal to noise ratio. In this work we develop a theoretical description of the inelastic scattering of EVB based on a combined multislice/Bloch-waves approach and explore quantitatively the usefulness of EVB for EMCD measurements. We conclude that vortex beams can provide an advantage over an intrinsic method only in an atomic resolution mode on crystalline samples.

I. INTRODUCTION

Electron magnetic circular dichroism (EMCD;[1]) as an experimental technique is known for about 7 years. During that time it went through a rapid development with significant improvements in spatial resolution and signal to noise ratio[2–5]. Early adopters have successfully used it in their applications. Yet, EMCD has not yet reached a stage of wide adoption as a routine characterization technique. The reasons are two-fold: 1) requirement of single-crystalline specimen precisely oriented in a two-beam or three-beam orientation, and 2) generally a low signal to noise ratio, which is due to the fact that EMCD needs to be measured aside the Bragg spots.

From this point of view, an introduction of electron vortex beams (EVB) into the transmission electron microscopy[6,7] has attracted a lot of attention, because in Ref.[7] it was experimentally demonstrated that using EVB one could measure EMCD with high signal to noise ratio, in principle even without requiring single-crystalline specimen. The recipe is simple: measure an electron energy loss spectrum (EELS) at a transmitted beam for an EVB with angular momentum $\langle \hat{L}_z \rangle = \hbar$ and another one for $\langle \hat{L}_z \rangle = -\hbar$ and their difference should provide an EMCD spectrum. Note that measurement at the transmitted beam means significantly stronger intensity (assuming that we can obtain EVB with an intensity comparable to an "ordinary" convergent electron beam).

Theoretical developments have followed[8–11], though quite surprisingly, further experimental results utilizing EVB for measurement of EMCD did not appear.

In this work we implement a theory of inelastic electron scattering for EVB, which is based on a combination of multislice[12] propagation method for the incoming beam and Bloch-waves (BW) description for the outgoing beam. The method is built on top of the efficient summation algorithm MATS[13] introduced recently. This code allows us to investigate the interaction between the EVB and magnetic atoms in the sample, providing unbiased estimation of the strength of the EMCD effect.

We argue that this is an optimal combination of methods because of 1) the complexity of the incoming beam, which would in BW method require a large number of independent directions of incoming wave-vectors, and that is elegantly solved by multislice method, and 2) after an inelastic event the propagation in various directions is incoherent and that can be naturally projected on BW fields corresponding to different outgoing plane-wave directions.

In the Section II we discuss the multislice simulation of the elastic propagation of the EVB through the sample with focus on exchange of angular momentum between the EVB and sample. Section III constitutes the main part of this manuscript. It consists of a theoretical subsection III A, where our simulation approach is explained, and of a simulation subsections III B and III C, discussing energy filtered diffraction patterns and high-resolution energy filtered images.

II. ELASTIC SCATTERING OF VORTICES

A. Multislice code and optimization of parameters

Here we summarize the basic formulation of the multislice method, following the book of E. J. Kirkland[12]. The vortex beam is treated by the time independent Schrödinger equation, with a relativistic mass m (1.39 times the rest mass of an electron with energy $E = 200$ keV)

$$\left[-\frac{\hbar^2}{2m}\nabla^2 - eU(x,y,z) \right] \psi(x,y,z) = E\psi(x,y,z), \quad (1)$$

where $\hbar$ is the reduced Planck's constant ($h/2\pi$) and $-eU$ is the potential energy of the electron ($e = |e|$, the magnitude of the charge of an electron). Assuming z direction to be the optic axis of the microscope, the total wave function $\psi(x,y,z)$ can be written as a product of a plane wave traveling in the z direction and a function $\phi(x,y,z)$, which changes slowly with z

$$\psi(x,y,z) = \phi(x,y,z)\exp\left(\frac{2\pi i z}{\lambda}\right), \quad (2)$$

where λ is the wave length of the electron, which is determined by the energy of the incident beam ($E = h^2/2m\lambda^2$ and $\lambda = 0.023$Å for a beam of energy 200 keV). Since we consider only the elastic scattering process, during the propagation the wave vector satisfies

$$k_x^2 + k_y^2 + k_z^2 = \frac{1}{\lambda^2}. \quad (3)$$

Inserting the wave function (Eq. 2) in Eq. 1, the Schrödinger equation for fast electrons moving in the z direction can be expressed as the following first order differential equation,

$$\frac{\partial \phi(x,y,z)}{\partial z} = \left[\frac{i\lambda}{4\pi} \nabla_{xy}^2 + i\sigma U(x,y,z) \right] \phi(x,y,z), \quad (4)$$

where $\sigma = 2\pi me\lambda/h^2$. The above equation is written ignoring the second order partial derivative of $\phi(x,y,z)$ with respect to z, because $\phi(x,y,z)$ is a slowly varying function in z direction, which implies that, $\left| \frac{\partial^2 \phi}{\partial z^2} \right| \ll \left| \frac{1}{\lambda} \frac{\partial \phi}{\partial z} \right|$ is a good approximation.

We have adopted a multislice method to solve for the wave function $\phi(x,y,z)$ from Eq. 4. The Coulomb potential of the specimen under investigation is sliced in multiple layers (spaced $\triangle z$ apart) perpendicular to the z axis. The incident wave enters the specimen from the top, transmits through a slice and then propagates a distance of $\triangle z$ to the next slice. The transmission-propagation process is continued until the wave exits the specimen. From Eq. 4, the wave function, after transmitting through a slice and propagating a distance of $\triangle z$, can be written as

$$\phi(x,y,z + \triangle z) = e^{\int_z^{z+\triangle z} \left(\frac{i\lambda}{4\pi} \nabla_{xy}^2 + i\sigma U(x,y,\tilde{z}) \right) d\tilde{z}} \phi(x,y,z). \quad (5)$$

For sufficiently small slice thickness $\triangle z$, the above equation can be expressed as,

$$\phi_{n+1}(x,y) = \exp\left(\frac{i\lambda\triangle z}{4\pi} \nabla_{xy}^2 \right) t_n(x,y)\phi_n(x,y), \quad (6)$$

where the $\phi_{n+1}(x,y)$ and $\phi_n(x,y)$ are the two dimensional wave functions at $z + \triangle z$ and z, respectively and $t_n(x,y)$ is called the transmission function, given by

$$t_n(x,y) = \exp\left(\int_z^{z+\triangle z} i\sigma U(x,y,\tilde{z}) d\tilde{z} \right). \quad (7)$$

Using Fourier transform, Eq. 6 can be written as,

$$\phi_{n+1}(x,y) = FT^{-1}\left\{ p(k_x,k_y,\triangle z) FT\left[t_n(x,y)\phi_n(x,y) \right] \right\}, \quad (8)$$

where FT refers to two dimensional Fourier transform and $p(k_x,k_y,\triangle z)$ is called the propagator function, given by

$$p(k_x,k_y,\triangle z) = \exp\left[-i\pi\lambda(k_x^2 + k_y^2)\triangle z \right]. \quad (9)$$

The incident beam is taken to be a vortex beam given by,

$$\phi(q,\varphi) = \exp(im\varphi)\Theta(q_{max} - q), \quad (10)$$

where φ and q are the azimuthal angle and radial vector in the condenser plane, respectively and Θ is the Heaviside function. Value of q_{max} is determined by the convergence semi-angle α and the electron wave vector $k(= 1/\lambda)$ and given by $q_{max} = k\alpha$. The initial wave function in the real space is obtained by Fourier transforming the above equation and then it is propagated through successive slices of the sample by applying Eq 8. The intensity of the wave function at various different thicknesses of the sample is shown in Fig 1.

Inelastic scattering simulations described in the next section are rather time consuming, optimization of computational parameters is of great importance. Major parameters for multislice part of the simulation are the sizes of the grids, both within a unit cell and the number of unit cells included in a simulation. We have adopted a grid of $42 \times 42 \times 42$ grid points within a single unit cell, which turned out to be sufficient to accurately reproduce a Bloch-waves calculation for a plane-wave illumination (see below).

The target maximum thickness in our simulations was 40nm, which means approximately 140 unit cells of bcc iron ($a = 2.87$Å). The number of unit cells in the x, y directions depends sensitively on the beam characteristics. For a plane wave $1a \times 1a$ is certainly enough. But for convergent beams (with or without angular momentum) that is not sufficient. Beam characteristics in our simulations are determined by the q_{max} parameter defined above. Small values of q_{max} mean a broad beam, which spreads very slowly, while large values of q_{max} produce very well focused beams, which however spread quickly as they propagate through the lattice. See Fig. 1, top panels, where a wide beam of diameter more than two unit cells does not spread much further within the lattice than its initial extent, even after 25nm of elastic propagation. On the other hand, a beam which is narrower than a projected interatomic distance can spread significantly. See the lower right panel, where the beam center is placed in between the atomic columns. On the other hand, passing this narrow beam via an atomic column pins it to it and its spreading into lateral coordinates seems to be minimal. That will turn out to be of importance, when analysing the energy filtered diffraction patterns, Sec. III B.

For determining the number of cells needed in the x, y direction we have selected the following criterion. We have propagated a vortex beam with angular momentum $+\hbar$ through 40nm of a free space (by setting the potential V to zero). When the beam starts overlapping with its periodic image, the angular momentum will start decreasing, because the tails from two neighboring simulation cells have opposite sense of the phase change. Thus following the thickness dependence of angular momentum $\langle \hat{L}_z \rangle$ of the beam wavefunction as a function of

(a) Top
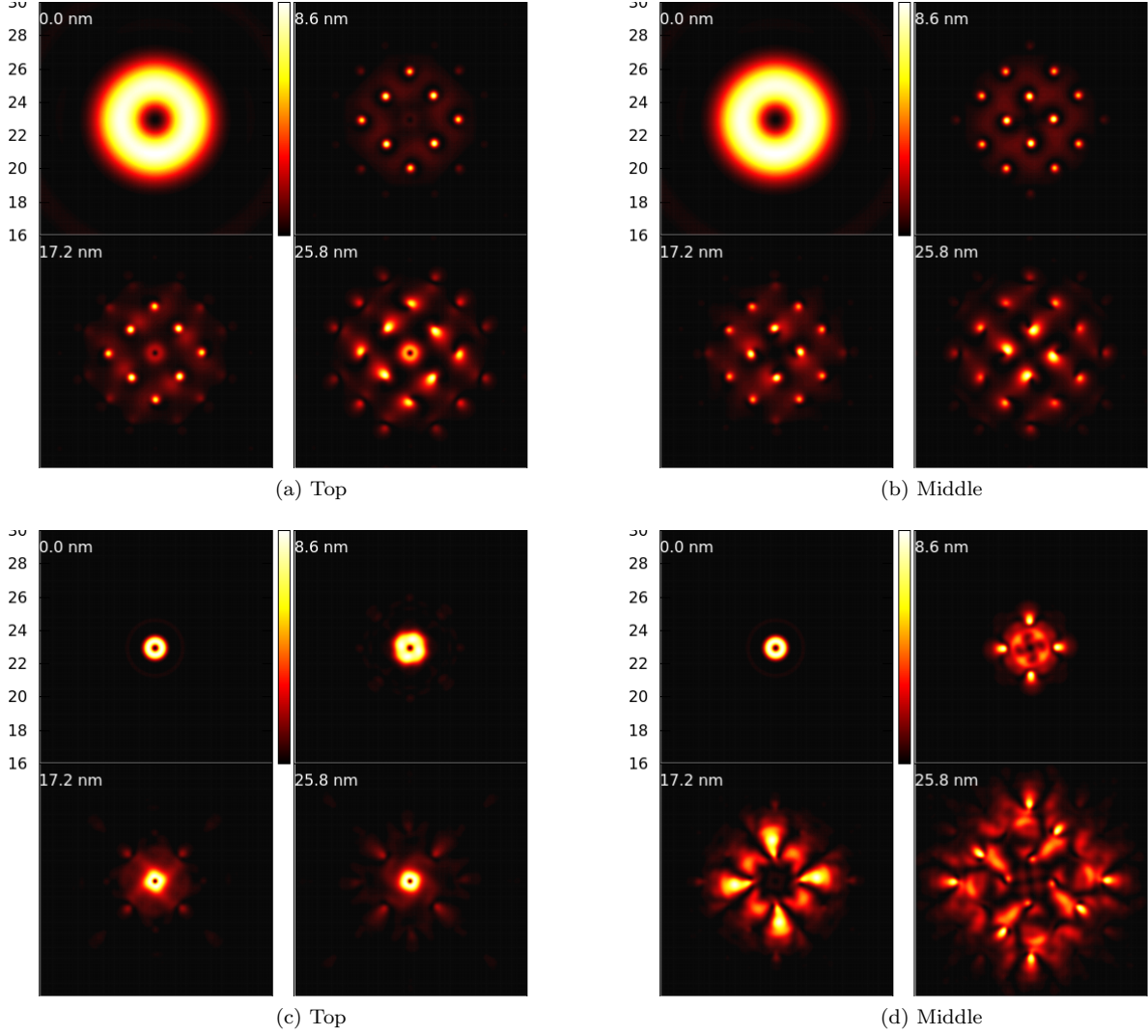

(b) Middle

(c) Top

(d) Middle

FIG. 1: Intensity of the electron beam at various different depths of the specimen, (a)-(b) for a wide beam ($q_{max} = 0.1$) and (c)-(d) for a narrow beam ($q_{max} = 0.5$). In (a) and (c), the beam is centered at the top of an atomic column and in (b) and (d), the beam is centered exactly at the middle of four adjacent atomic columns. The labels are given in the units of Å.

z-coordinate, we have determined the simulation box size needed to keep the $\langle \hat{L}_z \rangle$ constant within ±1%.

Note that the orbital angular momentum generally does not start from value of 1. This is caused by the initial normalization of the wavefunction and by the long tails of the vortex beam wavefunction, which originate from a sharp step-function-like cut-off in the **k**-space used in the construntion of the vortex beam wavefunction. This has some natural consequences. For small values of q_{max}, we get broad beams, which spread very little. Therefore, as long as the first donut-shaped maximum of EVB is deep inside the simulation box, we get a rather stable value of the orbital angular momentum. But a large simulation cell is needed to sufficiently contain the beam, i.e., to reach the $\langle \hat{L}_z \rangle \approx \hbar$. For example, $8a \times 8a$

shows a very stable value of the $\langle \hat{L}_z \rangle$, but the value itself is only $0.56\hbar$, indicating that a large proportion of the vortex wavefunction is outside the range of the simulation cell. For large values of the $q_{max} \gtrsim 0.5/a$ we obtain a narrow beam, which is usually well contained inside the simulation cell within the top slices. However, larger q_{max} also means faster spreading of the beam. For that reason, for example, the beam with $q_{max} = 1.0/a$ shows very stable $\langle \hat{L}_z \rangle$ up to a thickness of about 25nm, but then rapidly drops down. It appears that cell size of $16a \times 16a$ is sufficiently large to keep $\langle \hat{L}_z \rangle$ stable within ±1% for all tested values of q_{max}, except for the largest one $q_{max} = 1/a$, where the variation was about ±2%.
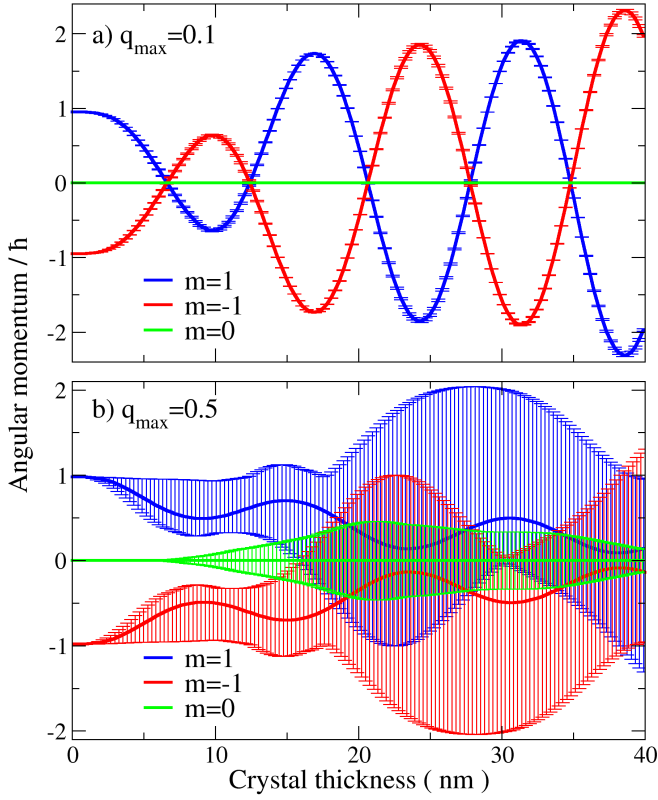
FIG. 2: Evolution of the orbital angular momentum of the vortex beam as a function of sample thickness, averaged over positions of the vortex core within a unit cell. Error bars indicate the spread of the angular momenta (minimum and maximum) for various positions of vortex core. Top panel shows a wide beam with $q_{max} = 0.1$ having virtually no dependence of angular momentum on the position of vortex core. For a narrow vortex beam (bottom panel, $q_{max} = 0.5$) there is a large spread of angular momenta.

B. Orbital angular momentum

We have performed two sets of simulations, namely one set for a narrow beam with $q_{max} = 0.5$ and another for a wide beam $q_{max} = 0.1$, respectively. These cases well represent the two limiting cases: 1) a beam that covers several unit cells and therefore might be rather insensitive to the precise position of the vortex center within the unit cell, and 2) a beam that is narrower than an interatomic distance—such beam would allow for a high-resolution TEM imaging of the sample. It has been demonstrated that sub-Ångström sized vortex probes can be obtained[19], therefore this limit describes a realistic scenario.

For both cases, we have performed a set of 36 calculations on a grid covering 1/8-th of an area of unit cell, one set for each of angular momenta $\langle \hat{L}_z \rangle = -\hbar, 0, \hbar$. Large size of our supercell allowed us to simulate thicknesses up to 40nm without loss of the normalization of
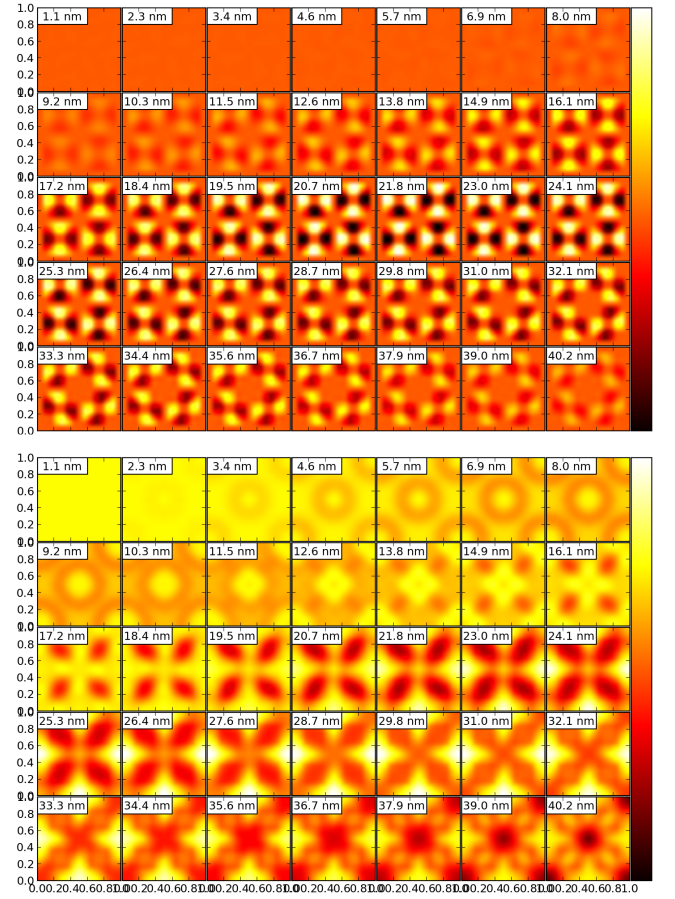

FIG. 3: Evolution of the orbital angular momentum of a narrow beam ($q_{max} = 0.5$) as a function of sample thickness and position of the vortex core within a unit cell. Top panel corresponds to a beam with zero angular momentum ($\langle \hat{L}_z \rangle = 0$, color bar ranges from $-0.5\hbar$ to $0.5\hbar$) and bottom panel is a vortex beam with unit angular momentum ($\langle \hat{L}_z \rangle = \hbar$, color bar range from $-2.3\hbar$ to $2.3\hbar$). Each square pattern maps shows a slice over a complete unit cell, thicknesses are in multiples of 4 unit cells, $4a \approx 1.15$nm.

the propagated electron probe wavefunction (change of norm below 10^{-4}).

The results of orbital angular momentum calculations are summarized in Figs. 2 and 3. As expected, the angular momentum of a wide beam practically does not depend on the illumination spot (Fig. 2, top panel), despite that the wavefunctions can differ substantially. The difference can be understood by comparing the intensities of the Fourier transformed wavefunctions for a wide beam, which show no difference for different illumination spot. The reciprocal space wavefunction in fact differ only by k_x, k_y-dependent complex phase factors of amplitude 1, originating from a shift theorem of discrete Fourier transform. In the real space these phase factors lead to non-trivial changes of the shape of wavefunction.

For a narrow beam, the picture is much more complex.

The exchange of angular momentum between beam and lattice sensitively depends on the illumination spot, as is indicated by the range of error bars in Fig. 2, bottom panel.

For the narrow beam, it is instructive to observe maps of the exchange of orbital angular momentum in the real space, as a function of sample thickness and beam vorticity. As already indicated by Fig. 2, for a narrow beam even the beam with zero angular momentum does exchange angular momentum with the lattice due to dynamical effects. At thicknesses beyond 10nm it acquires non-negligible angular momentum, peaking at around $0.5\hbar$ at thickness of 20nm. The maps of the angular momentum for $\langle \hat{L}_z \rangle = 0$ beam are shown in Fig. 3, in the top panel. As can be seen, the patterns of angular momentum are highly symmetric and areas of positive angular momentum are fully compensated by areas of negative angular momentum. As a result, an averaged value over the whole unit cell is zero at all thicknesses. On the other hand, these results indicate that for a sufficiently narrow beam, we can generate beam with angular momentum simply by passing it through a crystal of appropriate thickness at an appropriate position within the unit cell (assuming that such a task is or will be technically feasible).

A beam with orbital angular momentum $\langle \hat{L}_z \rangle = \hbar$ shows a different pattern, see Fig. 3 (bottom panel). The resulting patterns have different symmetry and in general, the average over the unit cell does not vanish, as is best seen from an averaged value in Fig. 2. As in the case of beam with $\langle \hat{L}_z \rangle = 0$, by illuminating an appropriate spot in the lattice for a sample of suitable thickness it is possible to manipulate the probe's angular momentum. However, the range of accessible values is substantially enhanced compared to a probe with zero initial angular momentum.

All the calculated 3-dimensional probe wavefunctions were stored and serve as an input for the calculations of the double-differential scattering cross-section in the next section.

III. INELASTIC SCATTERING OF VORTEX BEAMS

A. Theory

In this section we describe our method of calculating the dynamical diffraction effects and inelastic electron scattering for EVB. In fact, this method is applicable to illumination by an arbitrary coherent beam or a combination of beams, but here we restrict the treatment to the EVB with general value of $\langle \hat{L}_z \rangle$. We will consider core-level excitations of $2p$ electrons of bcc iron into unoccupied $3d$ states, i.e., the $L_{2,3}$ edge transitions.

In the Bloch waves (BW) formulation, the double-differential scattering cross-section (DDSCS) is given by

$$
\frac{\partial^2 \sigma}{\partial \Omega \partial E} = \sum_{\substack{jlj'l' \\ \mathbf{ghg'h'}}} C_{\mathbf{0}}^{(j)\star} C_{\mathbf{g}}^{(j)} D_{\mathbf{0}}^{(l)} D_{\mathbf{h}}^{(l)\star} C_{\mathbf{0}}^{(j')} C_{\mathbf{g'}}^{(j')\star} D_{\mathbf{0}}^{(l')\star} D_{\mathbf{h'}}^{(l')}
$$
$$
\times\, e^{i(\gamma^{(l)} - \gamma^{(l')})t} \frac{1}{N_{\mathbf{R}}} \sum_{\mathbf{R}} e^{i(\mathbf{q}-\mathbf{q'})\cdot\mathbf{R}}
$$
$$
\times\, \frac{1}{N_{\mathbf{u}}} \sum_{\mathbf{u}} \frac{S_{\mathbf{u}}(\mathbf{q},\mathbf{q'},E)}{q^2 q'^2} e^{i(\mathbf{q}-\mathbf{q'})\cdot\mathbf{u}} \tag{11}
$$

where

$$
\mathbf{q} = \mathbf{k}_{\text{out}} + \gamma^{(l)}\hat{\mathbf{n}}_{\text{out}} - \mathbf{k}_{\text{in}} - \gamma^{(j)}\hat{\mathbf{n}}_{\text{in}} + \mathbf{h} - \mathbf{g} \tag{12}
$$
$$
\mathbf{q'} = \mathbf{k}_{\text{out}} + \gamma^{(l')}\hat{\mathbf{n}}_{\text{out}} - \mathbf{k}_{\text{in}} - \gamma^{(j')}\hat{\mathbf{n}}_{\text{in}} + \mathbf{h'} - \mathbf{g'} \tag{13}
$$

The Bloch coefficients $C_{\mathbf{g}}^{(j)}, D_{\mathbf{h}}^{(l)}$ for incoming and outgoing beam, respectively, are indexed by beams $\mathbf{g}, \mathbf{h}$ and Bloch wave indices j, l. The elongations of the wave vectors perpendicular to the surface are denoted $\gamma^{(j)}, \gamma^{(l)}$ for incoming and outgoing Bloch waves, respectively. The t is the thickness of the crystal, $N_{\mathbf{R}}$ and $N_{\mathbf{u}}$ are number of unit cells and basis size. The mixed dynamical form-factor (MDFF) is denoted $S_{\mathbf{u}}(\mathbf{q},\mathbf{q'},E)$, where $\mathbf{q}, \mathbf{q'}$ and E are the momentum transfer vectors and energy loss, respectively. For more details about the theory of Bloch waves we refer the reader to original literature[15–17] or a more recent literature using the same notation[13,14].

A BW for incoming and outgoing beam can be expressed as

$$
\psi_{\text{in}}(\mathbf{r}) = \sum_{j\mathbf{g}} C_{\mathbf{0}}^{(j)\star} C_{\mathbf{g}}^{(j)} e^{i(\mathbf{k}_{\text{in}} + \gamma^{(j)}\hat{\mathbf{n}}_{\text{in}} + \mathbf{g})\cdot\mathbf{r}} \tag{14}
$$
$$
\psi_{\text{out}}(\mathbf{r}) = \sum_{l\mathbf{h}} D_{\mathbf{0}}^{(l)\star} D_{\mathbf{h}}^{(l)} e^{i(\mathbf{k}_{\text{out}} + \gamma^{(l)}\hat{\mathbf{n}}_{\text{out}} + \mathbf{h})\cdot\mathbf{r}} e^{i\gamma^{(l)}t} \tag{15}
$$

The incoming wave can be formally written as

$$
\psi_{\text{in}}(\mathbf{r}) = e^{i\mathbf{k}_{\text{in}}\cdot\mathbf{r}} \sum_{g_x, g_y} F_{g_x, g_y}^{(z)} e^{i(g_x x + g_y y)} \tag{16}
$$

where

$$
F_{g_x, g_y}^{(z)} = \sum_{jg_z} C_{\mathbf{0}}^{(j)\star} C_{\mathbf{g}}^{(j)} e^{i\gamma^{(j)} z} e^{ig_z z} \tag{17}
$$

implicitly assuming that $\hat{\mathbf{n}}_{\text{in}} = (0,0,1)$. Note that the $F_{g_x, g_y}^{(z)}$ is directly accessible from multislice calculation propagating the incoming beam, where $\{g_x, g_y\}$ correspond to a grid in the Fourier space.

We can accumulate the 2-dimensional arrays $F_{g_x, g_y}^{(z)}$ as a function of z, forming thus a 3-dimensional array with two dimensions in g_x, g_y and third dimension in z. A Fourier transform with respect to the z-coordinate will provide a 3-dimensional array $F_{\tilde{\mathbf{g}}}$ using which we can draw the following parallels with Bloch waves theory

$$
\psi_{\text{in}}(\mathbf{r}) = e^{i\mathbf{k}_{\text{in}}\cdot\mathbf{r}} \sum_{\tilde{\mathbf{g}}} F_{\tilde{\mathbf{g}}} e^{i\tilde{\mathbf{g}}\cdot\mathbf{r}} \tag{18}
$$
$$
\tilde{\mathbf{g}} \leftrightarrow \mathbf{g} + \gamma^{(i)}\hat{\mathbf{n}}_{\text{in}} \tag{19}
$$

finally allowing to write the following expression for DDSCS

$$\frac{\partial^2 \sigma}{\partial\Omega\partial E} = \sum_{\substack{\mathbf{h}\mathbf{h}'ll' \\ \tilde{\mathbf{g}}\tilde{\mathbf{g}}'}} F_{\tilde{\mathbf{g}}} D_{\mathbf{0}}^{(l)} D_{\mathbf{h}}^{(l)\star} F_{\tilde{\mathbf{g}}'}^{\star} D_{\mathbf{0}}^{(l')\star} D_{\mathbf{h}'}^{(l')}$$

$$\times\, e^{i(\gamma^{(l)}-\gamma^{(l')})t} \frac{1}{N_{\mathbf{R}}} \sum_{\mathbf{R}} e^{i(\mathbf{q}-\mathbf{q}')\cdot\mathbf{R}}$$

$$\times\, \frac{1}{N_{\mathbf{u}}} \sum_{\mathbf{u}} \frac{S_{\mathbf{u}}(\mathbf{q},\mathbf{q}',E)}{q^2 q'^2} e^{i(\mathbf{q}-\mathbf{q}')\cdot\mathbf{u}} \quad (20)$$

where

$$\mathbf{q} = \mathbf{k}_{\text{out}} + \gamma^{(l)}\hat{\mathbf{n}}_{\text{out}} - \mathbf{k}_{\text{in}} - \mathbf{h} - \tilde{\mathbf{g}} \quad (21)$$

$$\mathbf{q}' = \mathbf{k}_{\text{out}} + \gamma^{(l')}\hat{\mathbf{n}}_{\text{out}} - \mathbf{k}_{\text{in}} - \mathbf{h}' - \tilde{\mathbf{g}}' \quad (22)$$

Equation (19) deserves a few remarks. First, the grid of $\tilde{g}_z$ depends on the slice thickness and on total thickness of the simulated column. The number of slices per unit cell limits the HOLZ contributions included in the calculation (maximum $g_z = 2\pi/\Delta z$. In our calculations, we used 42 slices per lattice parameter, but for generating the $F_{\tilde{\mathbf{g}}}$ we only used 6 slices per lattice parameter in z-direction. Second, only wavelengths that are shorter than the column length can be recovered (minimum $g_z = 2\pi/t$). In our calculations we went up to approximately 40nm, but the fineness of the grid depends on the chosen thickness.

Having this in mind, the Bloch wave-vector elongations $\gamma^{(j,l)}$ are included via the $\tilde{g}_z$ values on the grid, as specified in the abovementioned Eq. (19). As a consequence, for a sufficiently large thickness this approach does not include any approximations and can fully recover the accuracy provided by Bloch waves method. This has been tested for a plane wave illumination and surprisingly, already for very thin specimen, both approaches provided very similar results.

Note further that vortex beam calculations simulated within a 16×16 supercell allow lateral components of the $\tilde{\mathbf{q}}$ to be fractions of the reciprocal lattice to the crystal unit cell. Summation over the lattice vectors $\mathbf{R}$ will however cancel out all terms for which $\mathbf{q} - \mathbf{q}'$ is not a reciprocal lattice vector of the unit cell. This consequence is equivalent to the incoherent summation over the illumination angle.

Concerning the high-resolution transmission electron microscopy simulation we add a technical remark of importance when shifting the beam position. This is implemented in the multislice code via shifting the potential instead and keeping the beam in the middle of the simulation cell. That has to be taken into account when combining it with Bloch waves in Eq. 20 via the shift theorem of discrete Fourier transform, which introduces phase factors for the Fourier components of the incoming waveunction.

The formulation in Eq. (20) also lends itself for a straightforward modification of the MATS summation algorithm[13], where the products $C_{\mathbf{0}}^{(j)\star} C_{\mathbf{g}}^{(j)}$ are replaced by $F_{\tilde{\mathbf{g}}}$, and $\mathbf{g}$ and $\gamma^{(j)}$ are extracted from $\tilde{\mathbf{g}}$ according
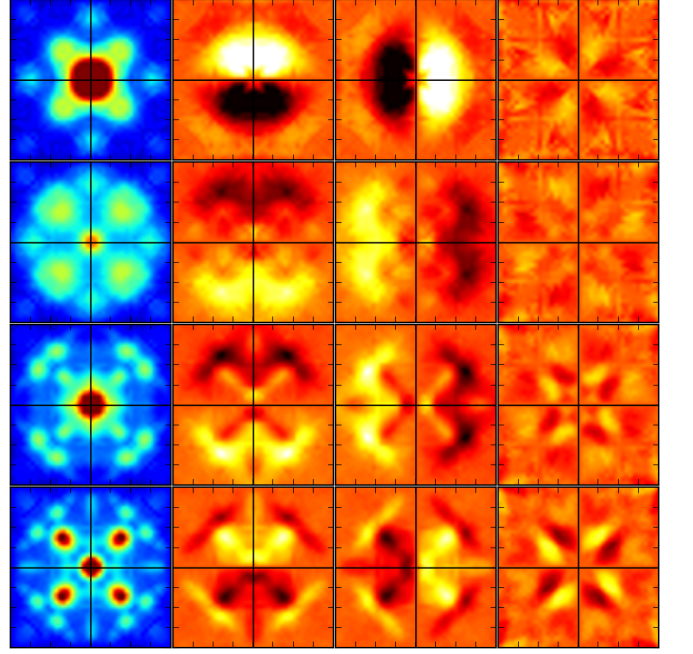

FIG. 4: Inelastic scattering of a wide vortex beam, $q_{\max} = 0.1$. Dependence on the angular momentum of the vortex beam as well as on the lateral position of the vortex core within the unit cell is negligible (see text for details). The grid of EFDIF patterns shows intensity per hole and per Bohr magneton of spin magnetization in x, y, z direction (columns from left to right) for four different thicknesses, 10nm, 20nm, 30nm and 40nm (rows from top to bottom). Range of plots is from $-2G$ to $2G$, where $\mathbf{G} = (100)$. The color scales are from 0 to 3.0 for the maps of n_h operator and -0.0625 to 0.0625 for maps of spin operators, respectively.

to Eq. (19). The first step of calculating an energy-filtered diffraction pattern is a multislice propagation of an electron beam wavefunction. This is followed by a post-processing code, which extracts the largest $F_{\tilde{\mathbf{g}}}$ and their corresponding $\tilde{\mathbf{g}}$ vectors, which are then mapped on a pair of $\mathbf{g}$ and $\gamma^{(j)}\hat{\mathbf{n}}_{\text{in}}$. Those are then loaded by the code that implements MATS algorithm as a complete information about the incoming beam wavefunction, and the rest (outgoing beam and summation) proceeds without any changes.

B. Energy filtered diffraction patterns

In a recent manuscript[18] it was shown how to decompose the MDFF into a set of terms, each based on a ground state expectation value of certain local electronic structure property, such as number of holes, spin moment along x, y, z directions, orbital or spin-magnetic anisotropy and spin-orbital coupling. This allows to evaluate a set of so called "operator maps" for inelastic electron scattering, which would represent a normalized con-
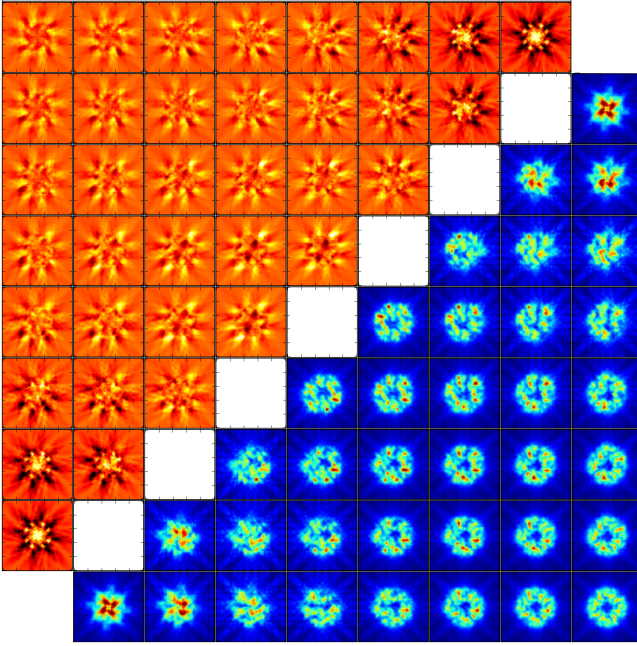
FIG. 5: Inelastic scattering of a narrow vortex beam with $q_{max} = 0.5$ with angular momentum $\langle \hat{L}_z \rangle = +\hbar$ for a sample thickness of 20nm. Figure displays a grid of calculated EFDIF patterns corresponding to the intensity per hole (right-bottom triangle) and per Bohr magneton in z-direction (left-top triangle). The color scales are from 0 to 1.2 for maps of n_h operator and -0.025 to 0.025 for maps of s_z operator, respectively. The range of plots is from $-5G$ to $5G$, where $\mathbf{G} = (100)$ in both x and y directions. The maps in the lower left corner correspond to a vortex core passing through an atom at the origin of unit cell, while the maps in right top corner describe a vortex passing through a column of atoms in the centers of the cubic cell.

tribution of let's say spin along y-direction to the scattering cross-section. Here we adopt this method and evaluate "operator maps" for an L_3 edge in a bcc structure with a lattice parameter of bcc iron. We have evaluated operator maps normalized per hole in the $3d$ shell and per Bohr magneton of spin magnetization separately in x, y and z direction. Knowing the expectation values of these properties, we can recover the complete diffraction pattern as a linear combination of these four maps, e.g., if magnetization points along z direction then

$$\int_{L_3} \frac{\partial^2 \sigma}{\partial \Omega \partial E} dE \approx 3.7 O_{n_h}^{L_3}(\Omega) + 2.3 O_{s_z}^{L_3}(\Omega) \qquad (23)$$

where Ω is the scattering angle, O_{n_h} and O_{s_z} are the normalized operator maps for number of holes n_h and spin magnetization s_z operators, and 3.7 and 2.3 are the ground state expectation values of n_h and s_z for bcc-iron[18].

We have evaluated energy filtered diffraction patterns (EFDIF) for both vortex diameters at all 36 positions

within the unit cell that were introduced in the Sec. II B. However, due to large computational demands, we only evaluated EFDIF patterns at four different thicknesses, namely at 36, 68, 104 and 140 unit cell in z-direction, which approximately corresponds to thicknesses 10nm, 20nm, 30nm and 40nm, respectively.

First we discuss the results for the wide vortex beam, $q_{max} = 0.1$. The orbital angular momenta were almost insensitive to the position of the vortex center within the unit cell (Sec. II B), simply because the vortex beam covers more than just one column of atoms (in fact its diameter is larger than a unit cell). Therefore one may expect a small sensitivity of the dynamical diffraction effects as a function of the position of vortex center within the unit cell. Similar reasoning applies for the inelastic scattering. Indeed, the results show that the EFDIF patterns are independent of the position of the vortex center, and, moreover they are independent of the angular momentum of EVB. The individual EFDIF patterns are shown in Fig. 4. In this sense, for a wide vortex beam there is no contribution of the beam vorticity to the observed EMCD signal. Note that there is a non-negligible magnetic signal present in the diffraction plane for all three directions of magnetization. However, this solely originates from dynamical diffraction effects and is an "ordinary" (or intrinsic) EMCD. In the light of these findings, we suggest that the EMCD signal observed in[7] was of intrinsic origin.

For a narrow vortex beam we observe a much more rich behavior. As already indicated by the calculations of the angular momentum, there is a complicated exchange of angular momentum between the beam and sample, sensitively depending on the position of the vortex center within the unit cell. We show a summary of calculations of the intensity of scattered electrons per hole and per $1\mu_B$ of spin magnetization in z-direction in Fig. 5. The figure shows EFDIF patterns for all treated positions of the vortex core for a beam with $\langle \hat{L}_z \rangle = \hbar$. The development of the shape of the diffraction pattern is rather non-trivial, both for the non-magnetic and magnetic contribution. Magnetic signal indeed survives within the diffraction plane and at certain vortex positions is rather strong, especially close to the atom columns (bottom-left and top-right corner of Fig. 5). A quantitative analysis of the strength of magnetic signal follows in the next subsection.

C. High-resolution energy-filtered TEM images

The evaluated EFDIF patterns allow for an extraction of high-resolution energy-filtered images (HR-EFI) by selecting an appropriate detection aperture size. Recently, Prange et al. have calculated energy-resolved high-resolution images[20], however they have focused on a simulation for a standard STEM probe beam using the Bloch waves method. Our approach of using multislice for the incoming beam offers an alternative approach.
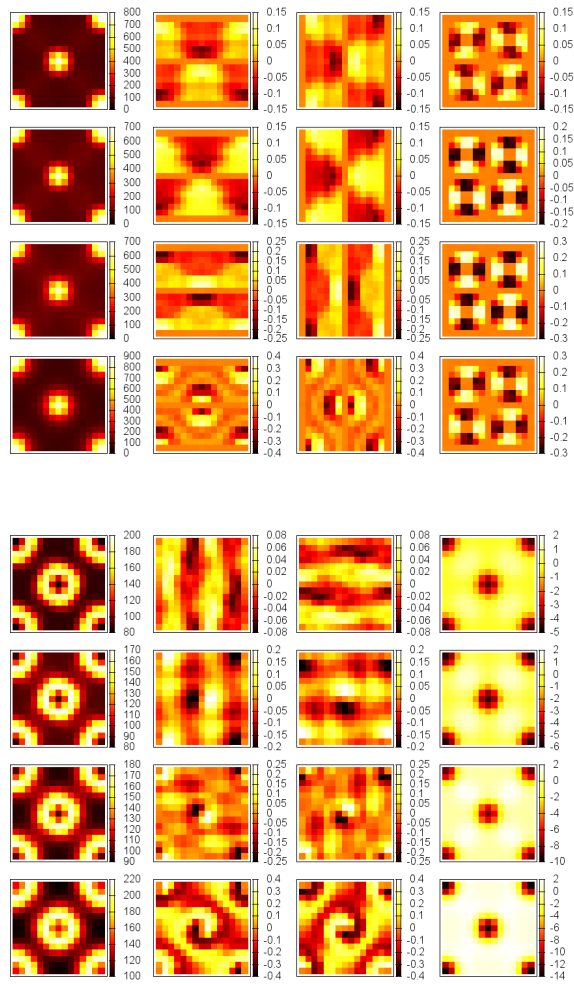
FIG. 6: High-resolution energy-filtered images for a beam of zero angular momentum (top panel) and $\langle \hat{L}_z \rangle = \hbar$ (bottom panel). Individual rows correspond to approximate thicknesses of 10nm, 20nm, 30nm and 40nm, respectively, and columns refer to a signal contributions normalized per hole or per $1\mu_B$ of spin magnetization along x, y, z directions, respectively. Each pattern shows an x, y plane within a unit cell.

We simulated the detector aperture by a circle of radius $0.5G$ or $3.2G$ for the $q_{max} = 0.1$ or 0.5, respectively.

The calculations for a wide beam expectedly do not produce any contrast due to a probe size larger than interatomic distances. The non-magnetic signal is a flat function of a position of the vortex core and magnetic signal vanishes after integration over an aperture. A non-trivial observation is that the EFDIF patterns do not depend on the vorticity either. Therefore wide vortex beams can't offer any improvement of detection of EMCD signal over an intrinsic method. For the narrow beam ($q_{max} = 0.5$) we plotted the resulting HR-EFI in Fig. 6 for all four thicknesses and separately the contributions from n_h and $s_{x,y,z}$.

The results for beam with zero angular momentum show well-resolved positions of atomic columns. A nonzero magnetic signal can be detected within the diffraction plane, however it is of negligible relative magnitude well below 1%.

In the case of vortex beam ($\langle \hat{L}_z \rangle = \hbar$) the maximum strength of the non-magnetic signal is much lower. It can be explained by a more spread beam due to its doughnut shape, which also leads to a lower spatial resolution—note how much wider are the atomic columns in the HR-EFI for a vortex beam, compared to a beam with zero angular momentum with the same q_{max}. On the other hand, the magnetic signal is much stronger, at certain probe positions reaching up to around 10%. This finding would suggest that for a sufficiently narrow vortex beam channeling through a column of atoms, the intensity of inelastically scattered electrons in the forward direction is substantially influenced by magnetic properties of the atomic column. Measuring at the transmitted beam would mean much stronger magnetic signal intensity relative to the intensity of incoming beam, when compared to the intrinsic EMCD.

Importantly, an integral of HR-EFI over the area of unit cell provides negligible magnetic signals of the order of less than 0.01% of the non-magnetic signal. Therefore our calculations suggest that for measurement of EMCD with vortex beams one has to use beams allowing to reach an atomic resolution. As a consequence, although the EMCD spectrum shown in Ref. 7 is most likely of an intrinsic nature, there is a theoretical possibility to measure enhanced magnetic signal with vortex beams, but this is yet to be demonstrated experimentally.

IV. CONCLUSIONS

We have evaluated inelastic scattering of electron vortex beams on matter, including dynamical diffraction effects. Our analysis of energy-filtered diffraction patterns and high-resolution energy-filtered images suggests that in order to observe a magnetic signal, the vortex beam must reach a diameter allowing an atomic resolution and pass through a column of atoms carrying the magnetic moment. Averages over the unit cell provide negligible net magnetic signal, regardless of the diameter of the vortex beam.

V. ACKNOWLEDGEMENTS

[1] P. Schattschneider, S. Rubino, C. Hébert, J. Rusz, J. Kuneš, P. Novák, E. Carlino, M. Fabrizioli, G. Panaccione and G. Rossi, Nature **441**, 486 (2006).

[2] P. Schattschneider, C. Hébert, S. Rubino, M. Stöger-Pollach, J. Rusz and P. Novák, Ultramicroscopy **108**, 433 (2008).

[3] B. Warot-Fonrose, F. Houdellier, M.J. Hytch, L. Calmels, V. Serin, and E. Snoeck, Ultramicroscopy **108**, 393 (2008).

[4] P. Schattschneider, M. Stöger-Pollach, S. Rubino, M. Sperl, Ch. Hurm, J. Zweck, and J. Rusz, Phys. Rev. B **78**, 104413 (2008).

[5] H. Lidbaum, J. Rusz, S. Rubino, A. Liebig, B. Hjörvarsson, P. M. Oppeneer, E. Coronel, O. Eriksson, and K. Leifer, Ultramicroscopy **110**, 1380 (2010).

[6] M. Uchida and A. Tonomura, Nature **464**, 737 (2010).

[7] J. Verbeeck, H. Tian, and P. Schattschneider, Nature **467**, 301 (2010).

[8] S. M. Lloyd, M. Babiker, and J. Yuan, Physical Review A **86**, 023816 (2012).

[9] S. M. Lloyd, M. Babiker, and J. Yuan, Physical Review Letters **108**, 074802 (2012).

[10] S. Löffler, P. Schattschneider, Acta Cryst. A**68**, 443-447 (2012).

[11] J. Yuan, S.M. Lloyd, M. Babiker, arXiv:1303.5322.

[12] E. J. Kirkland, *Advanced Computing in Electron Microscopy*, 2nd edition, Springer (2010).

[13] J. Rusz, S. Muto, K. Tatsumi, accepted to Ultramicroscopy, arXiv:1206.5843v1 [cond-mat.mtrl-sci].

[14] J. Rusz, S. Rubino, and P. Schattschneider, Phys. Rev. B **75**, 214425 (2007)

[15] C. J. Rossouw, and V. W. Maslen, Phil. Mag. A **49**, 743-757 (1984).

[16] H. Kohl, and H. Rose, Advances in Electronics and Electron Optics **65**, 173-226 (1985).

[17] D. K. Saldin, Phil. Mag. B **56**, 515-525 (1987).

[18] J. Rusz, S. Rubino, O. Eriksson, P. M. Oppeneer, K. Leifer, Phys. Rev. B **84**, 064444 (2011).

[19] J. Verbeeck, P. Schattschneider, S. Lazar, M. Stöger-Pollach, S. Löffler, A. Steiger-Thirsfeld, and G. Van Tendeloo, Appl. Phys. Lett. **99**, 203109 (2011).

[20] M. P. Prange, M. P. Oxley, M. Varela, S. J. Pennycook, and S. T. Pantelides, Phys. Rev. Lett. **109**, 246101 (2012).